Published in final edited form as:

Nat Nanotechnol. 2017 February 07; 12(2): 106–117. doi:10.1038/nnano.2016.301.

Utilizing the power of Cerenkov light with nanotechnology

Travis M. Shaffer[1,2,3], **Edwin C. Pratt**[4], and **Jan Grimm**[1,2,4,5,*]

[1]Molecular Pharmacology Program, Memorial Sloan Kettering Cancer Center, New York, New York 10065, USA.

[2]Department of Radiology, Memorial Sloan Kettering Cancer Center, New York, New York 10065, USA.

[3]Department of Chemistry, Hunter College and Graduate Center of the City University of New York, New York, New York 10065, USA.

[4]Department of Pharmacology, Weill Cornell Medical College, New York, New York 10021, USA.

[5]Department of Radiology, Weill Cornell Medical College, New York, New York 10021, USA.

Abstract

The characteristic blue glow of Cerenkov luminescence (CL) arises from the interaction between a charged particle travelling faster than the phase velocity of light and a dielectric medium, such as water or tissue. As CL emanates from a variety of sources, such as cosmic events, particle accelerators, nuclear reactors and clinical radionuclides, it has been used in applications such as particle detection, dosimetry, and medical imaging and therapy. The combination of CL and nanoparticles for biomedicine has improved diagnosis and therapy, especially in oncological research. Although radioactive decay itself cannot be easily modulated, the associated CL can be through the use of nanoparticles, thus offering new applications in biomedical research. Advances in nanoparticles, metamaterials and photonic crystals have also yielded new behaviours of CL. Here, we review the physics behind Cerenkov luminescence and associated applications in biomedicine. We also show that by combining advances in nanotechnology and materials science with CL, new avenues for basic and applied sciences have opened.

In 1888, the accomplished physicist Oliver Heaviside presented a prescient theoretical argument: luminescence would occur from the interaction of charged particles travelling faster than the phase velocity of light with surrounding matter[1]. In 1896, Henri Becquerel discovered that gamma rays were emitted by uranium, ushering in the field of nuclear physics. Over four decades after Heaviside's original hypothesis, Pavel Cerenkov (the other spelling used is Cherenkov), a Russian postgraduate student in physics under Sergei Ivanovich Vavilov, investigated the luminescence of uranyl salt solutions under the gamma-ray irradiation of radium placed directly under his solutions. In autumn 1933, his solution accidentally contained the solvent (sulfuric acid) alone, yet he observed the very same glow

*Correspondence should be addressed to J.G. grimmj@mskcc.org.

Competing financial interests

The authors declare no competing financial interests.

from the radium emissions[2]. Vavilov and Cerenkov determined that the luminescence resulted from solvent interaction with the high-energy Compton electrons resulting from the gamma rays of radium[3]. In 1937, Ilya Frank and Igor Tamm, working in the same laboratory, published the classical theory behind Cerenkov's observations[4,5], with Vitaly Ginzburg publishing a quantum description soon after[6].

Physics behind Cerenkov luminescence

Owing to the various mechanisms by which high-energy subatomic particles reach an energetic equilibrium with their surroundings, determining how luminescence is produced from these interactions was no easy task. For this Review, we limit discussion to beta (β) particles (that is, electrons and positrons, the positively charged antimatter counterpart of the electron) as most CL emitters used in nanoscience originate from β-emitting radionuclides or electron beams. For a more general consideration of other high-energy particle (for example, α-particles) and gamma interactions with matter, we recommend a recent comprehensive text[7]. Here, we use the classical description of the Cerenkov mechanism (that is, treating the β-particle as a point charge), which most CL research has been based on. Notably, recent work has demonstrated that treating the Cerenkov mechanism as a quantum wavepacket results in certain deviations from the classical description, such as spectral cut-offs and discontinuity[8].

The CL mechanism involves polarization of the atoms in the traversed medium, with subsequent relaxation of the induced dipole state back to baseline (Fig. 1a)[9,10]. As the charged particle travels faster than the speed of light in the medium, there is a coherent wavefront, as described by Huygens's principle (Fig. 1b), resulting in emission of photons. These emitted photons propagate at a forward angle in the particle's direction of travel (Fig. 1c) in materials with positive refractive indices. This angle (θ) is dependent on the kinetic energy of the charged particle (β) and the refractive index (n) at a specific frequency (ω) and is defined in equation (1). Through this relationship, determining the Cerenkov cone angle allows calculation of the charged particles' energy.

$$\cos\theta = \frac{1}{\beta n(\omega)} \quad (1)$$

The relationship describing the Cerenkov threshold (that is, the energy necessary to generate CL) is described in equation (2), where the velocity (v) of a charged particle must equal or exceed the phase velocity of light (c) in the medium. Cerenkov light is generated when this relationship is met.

$$\beta = \frac{v}{c} \geq \frac{1}{n} \quad (2)$$

The photon flux resulting from the Cerenkov mechanism is described by the Frank–Tamm equation (equation (3)):

$$\frac{\mathrm{d}N}{\mathrm{d}x}=2\pi\alpha\left(1-\frac{1}{\beta^2 n^2}\right)\int_{\lambda_1}^{\lambda_2}\frac{1}{\lambda 2}\mathrm{d}\lambda \quad (3)$$

Here, the photon flux per distance (dN/dx) is dependent on the wavelengths of interest (λ_1 λ_2), the velocity of the charged particle (β^+ or β^-) relative to the speed of light and the refractive index (n) of the material through which the charged particle passes, with the fine structure constant $\alpha = e^2/(4\pi\varepsilon_0)\hbar c$ (≈1/137), where e is the electron charge, ε_0 is the permittivity of free space, and $\hbar$ is the reduced Planck constant. The Cerenkov spectrum is continuous in the visible region, decreasing in a $1/\lambda^2$ relationship from the ultraviolet/blue range to the visible range[11]. In the X-ray region of the spectrum, n falls below unity and therefore CL ceases[12].

With increasing n of the traversed matter, the Cerenkov threshold decreases. Subatomic particles emitted during radioactive decay produce a wide range of energy spectra, with some particles under the Cerenkov threshold (261 keV for electrons and positrons in water) and some exceeding it. From the Frank–Tamm equation, a singly charged particle travelling at c (that is, $\beta = 1$) emits 320 photons in the visible spectrum per centimetre of water[13]. With a higher n, there is a greater difference in the phase velocity of light and the particle velocity, resulting in increased photon flux[12]. While n values are often assumed to be constant over the visible spectrum in biomedical CL research, the n of a material in reality varies with frequency. This dependence on n is, in general, often ignored in biomedical imaging, however, the importance of n in CL intensity is seen in the Frank–Tamm equation.

While these descriptions are useful for most materials, they break down when describing metamaterials, which are composite synthetic materials engineered through nanofabrication or self-assembled nanoparticles to form an object with properties not seen in nature. For any material, n can be expressed as the product of permittivity (ε) and permeability (μ) shown in equation (4); when both are negative, it is considered a double negative material. In traditional optics, n is the ratio of the speed of light in a vacuum to the phase velocity of light in the particular medium. When a beam of light passes between media with different n, it refracts at an angle to the normal and is quantified in equation (5). The normal line is often represented as a second beam of light that travels unaltered through the medium. Based on the Fresnel equations, Snell's law assumed a positive n for all materials found in nature, as light would be refracted at a positive sine angle ($\sin\theta_1 > 0$). In contrast, negative index materials (NIMs) refract light and produce a negative sine angle ($\sin\theta_2 < 0$).

$$n^2=\varepsilon\mu \quad (4)$$

$$\frac{n_1}{n_2}=\frac{\sin\theta_1}{\sin\theta_2} \quad (5)$$

For CL applications, metamaterial structures contain periodic subdiffraction dimensions whereby the material can behave like plasma at a particular frequency. The plasmonic behaviour allows magnetic and electrostatic properties to be decoupled, giving rise to novel properties, such as a negative n. CL generation in a NIM can occur much like in a traditional material when $n^2(\omega) > 1$ when $\beta = 1$, yet the direction of the light cone is in the opposite direction (Fig. 1d), as for traditional CL (that is, backwards and not in the direction of the particle's path). Outside of the plasmonic frequency range, the metamaterial behaves as a normal material. NIMs are of particular use with CL, as the reversed cone angle yields a wider range to measure compared with traditional materials, which are limited between 0° and 90°. This wider angle range allows NIMs to be used as more accurate detectors since the photon emission angle is related to the particle velocity from equation (1).

To summarize, atoms in the traversed medium are polarized by a charged particle's field, and emit photons due to coherence when the polarized atoms return to their original state. Higher particle velocities and refractive indices of the medium result in the emission of more photons, with the Cerenkov light ultraviolet-weighted. In metamaterials, traditional equations modelling Cerenkov behaviour break down, as the interactions assumed for traditional materials are no longer true. This leads to interesting phenomena, such as the lack of a Cerenkov cut-off energy. These are discussed at the end of this Review.

Cerenkov imaging using clinical agents

Until the turn of the twenty-first century, most experimental Cerenkov applications consisted of detection of cosmic particles such as gamma rays and hadronic cosmic rays[14] or particle velocity calculations using the angle of emitted Cerenkov light. The mid-twentieth century brought the discovery of both the antiproton[15] and the heavy particle J/ψ[16,17], aided by unique Cerenkov characteristics. While CL has long been utilized in particle physics, the implications of the Cerenkov phenomenon for *in vivo* biomedical research with radionuclides were recognized only in 2009. Robertson *et al.* first observed CL originating from an animal injected with a clinical radiotracer and designated the technique Cerenkov luminescence imaging (CLI)[18]. Following this demonstration of the feasibility of imaging CL with pre-clinical optical imaging instruments, the Cerenkov characteristics of numerous medical radionuclides were investigated[19–21]. CL therefore allows optical imaging of clinical radiotracers, providing a unique multimodal system where the same agent is detectable with two independent modalities (optical and positron emission tomography (PET) imaging). This offers several advantages and compliments traditional nuclear imaging. (1) Optical cameras are much more cost-effective than expensive nuclear imaging instruments. (2) Imaging times for CLI are typically much shorter. (3) Several subjects can typically be imaged in parallel preclinically using optical systems. (4) Radionuclides that are currently quite difficult to image *in vivo* may be quantitatively imaged using CL. This is an area of great potential for CLI, as radionuclides such as yttrium-90 (^{90}Y)[22] or actinium-225 (^{225}Ac)[23] (an α-emitter with β^--emitting daughters) are quite difficult to image otherwise. These radionuclides, used for therapy, could be combined with fluorescent nanoparticles or dyes to enable optical readouts superior to current imaging techniques. Besides the opportunity of using clinical radiotracers for optical imaging, CL also offers opportunities to implement unique imaging and therapeutic systems in combination with nanoparticles. As

radionuclides such as fluorine-18 (^{18}F) are routinely used for cancer diagnosis, the majority of CL studies are in oncological research.

While CL has already been used for non-invasive imaging in patients[24,25] and extensively in preclinical models using clinically available radiotracers, the field had to overcome various challenges. The first is the CL spectrum, which has the highest intensity in the ultraviolet region and rapidly decreases at longer wavelengths. The $1/\lambda^2$ relationship of CL is shown using a preclinical imaging scanner (IVIS Spectrum) in Fig. 2a. Preclinical optical scanners (namely the IVIS family of scanners) with calibrated filters from 500 to 840 nm are often used in these preclinical studies, as they are widespread due to their use in fluorescence and bioluminescence imaging. As tissue absorption and scattering is highest at shorter wavelengths (Fig. 2b), detection of CL deeper than a few centimetres is difficult. Another major challenge is the low level of CL (about one billion times less than ambient light)[26]. This very low photon flux means that ambient light needs to be blocked and long acquisition times of several minutes are required to obtain acceptable signal to background.

Nanoparticles and CL in life sciences

The ultraviolet-weighted spectrum of CL has found an ideal partner in nanoparticles, namely in secondary Cerenkov emission fluorescence imaging (SCIFI)[27] or the synonymous Cerenkov radiation energy transfer (CRET)[28]. Here, the decay of a radionuclide generates CL, which subsequently interacts with a nanoparticle, commonly one that exhibits photoluminescence resulting in the emission of longer-wavelength photons (Fig. 3a). Nanoparticles are best suited for use with CL given their high optical cross-sections compared with single small-molecule fluorophores. Insulating and semiconducting nanoparticles, such as metal oxides, are best for CL, as visible photons can be absorbed and reemitted by the nanoparticle unlike most metallic nanoparticles, which only absorb. Photon modulation in metal oxides and quantum dots (QDs) can be performed through altering the density of states by quantum confinement, imbuing tunable properties based on size and shape. Due to their excitation by blue light, high quantum yield and large Stokes shifts, QDs are the ideal nanopartners for pairing with Cerenkov emitters. The combination results in a significant redshift of the original CL signal, which allows for better *in vivo* imaging due to the superior tissue penetration in that part of the spectrum[29]. SCIFI also forfeits the need for external excitation light as the excitation originates internally from the injected radiotracer, reducing autofluorescence of tissue and improving signal to background ratios. This in turn allows superior signal depth penetration and sensitivity when compared with standard fluorescence imaging[27]. Nanoparticle–Cerenkov systems can be broadly grouped into three categories: Cerenkov emitters separate from nanoparticles, emitters bound to the nanoparticle surface and emitters incorporated into the nanoparticle lattice (Fig. 3b).

When combining a nanoparticle with a radionuclide for CL, a few considerations are necessary. First, the choice of radionuclide will greatly affect the CL intensity. If high-intensity CL is necessary, radiotracers such as gallium-68 (^{68}Ga) or ^{90}Y would be preferable to ^{18}F or copper-64 (^{64}Cu). If the application involves increasing depth penetration of CL, a photoluminescent nanoparticle with a high quantum yield that is excited by the blue-weighted CL and emits in the red or near-infrared (where tissue is less absorbent) is

preferable. Table 1 shows examples of clinical radionuclide–nanoparticle pairings, along with Cerenkov photons per disintegration of common β-emitters.

Early work combining nanoparticles and Cerenkov emitters utilized the widespread clinical PET radiotracer 2-deoxy-2-(^{18}F) fluoro-D-glucose ([^{18}F]-FDG) together with QDs. The Cerenkov spectrum of [^{18}F]-FDG alone showed the characteristic $1/\lambda^2$ spectrum, whereas QDs mixed with [^{18}F]-FDG showed a decrease in the ultraviolet region and a peak in the red region, corresponding to the expected shift[28]. This peak receded once the [^{18}F]-FDG decayed. Liu *et al.* expanded this concept to investigate three CdSe–ZnS core–shell QDs (QD655, QD705 and QD800) with the β^--tracer iodine-131 (^{131}I), both *in vitro* and *in vivo*. The QD–^{131}I solutions exhibited much higher optical intensities *in vivo* than ^{131}I alone due to the redshifted spectrum, demonstrating the utility of SCIFI to modulate CL into light that is more penetrating through tissues. The QDs allowed multiplexed optical imaging due to the separate emission peaks of each QD (Fig. 4a–d)[29].

In an interesting expansion on the concept of SCIFI, Hu *et al.* demonstrated that rare-earth europium oxide nanoparticles can be excited by multiple interactions between radionuclides and europium oxide nanoparticles. These interactions involve not only visible photons from the Cerenkov mechanism in an aqueous solution of [^{18}F]-FDG but also gamma-ray photons such as the 511 keV photons from positron annihilation originating from ^{18}F or 140 keV photons from technetium-99m (^{99m}Tc)[30]. The authors coined this technique radiopharmaceutical-excited fluorescence imaging (REFI), which operates via a similar mechanism as previous work with dual-excited, rare-earth microparticles[31]. Through excitation by both mechanisms, the depth of imaging in tissue phantoms (artificial tissue mediums that mimic the absorption and scattering of tissue) and *in vivo* was shown to be superior compared with only CL (Fig. 4e–h). As these nanoparticles utilize both gamma and Cerenkov photons for a greater optical signal intensity and depth penetration, the combination of radiotracers and rare-earth nanoparticles for *in vivo* optical imaging is an area ripe for further investigation.

While pairing clinical radiotracers with nanoparticles is attractive due to availability and easier clinical translation, both entities (nanoparticle and radionuclide) need to co-localize to obtain the desired effect. While this is easily accomplished *in vitro*, it presents a challenge for *in vivo* applications. As tissue absorbs much of the ultraviolet-weighted Cerenkov light, and typical Cerenkov thresholds for ^{18}F are only met for less than a millimetre distance travelled by the positron before annihilation[21], appreciable tumour uptake of both probes is necessary to see the desired wavelength shift. To circumvent this, radiotracers can be attached directly to the surface of the nanoparticle, which are capable of high cargo loads. This concept abrogates the disadvantageous necessity of co-localization of the particle and the radiotracer *in vivo* at the same point in time and space, but also results in possibly undesired signal from nonspecific distribution. To this end, a variety of nanoparticles have been developed, all carrying their own radionuclide as an internal excitation beacon. Typical methods of radiotracer attachment include a chelator or prosthetic group attached to a nanoparticle surface coating[32], liposomes or micelles that contain both nanoparticles and the radiotracer[33,34], and up-converting porphyrin-phospholipid-coated inorganic nanoparticles[35]. Recent work has optimized radiometal attachment to nanoparticles without

the need for surface modification with a chelator or prosthetic group[36]. A variety of particles, including amorphous silica nanoparticles[37–39] and iron oxide nanoparticles[40], have been radiolabelled with multiple radiotracers in this way.

Demonstrating this principle, superparamagnetic iron oxide nanoparticles were radiolabelled with ^{68}Ga for triple-modal (PET/MR/CLI) sentinel lymph node imaging, where MR is magnetic resonance. With the high CL intensity of ^{68}Ga due to its high β^+ energy, Cerenkov luminescent-guided resection could be possible[41]. The PET tracer iodine-124 (^{124}I) (half-life, $t_{1/2}$ = 4.2 d) has been used to radiolabel gold nanoparticles[42,43] and liposomes[33] for dual-modal CL and PET imaging, allowing later imaging time points. As liposomes such as Doxil and Caelyx are already approved by the US Food and Drug Administration for drug delivery, their use in imaging is attractive for clinical translation[44]. In another radioiodine nanosystem, biodegradable nanoparticles were used to transfect plasmid DNA into the lungs of mice with *in vivo* biodistribution followed serially using both PET and CLI, highlighting the increased prevalence of CL in biological studies[45].

An interesting hybrid system of microspheres that contained a high-refractive-index liquid (n = 1.54) and QDs was recently developed[46]. QDs were loaded together with wintergreen oil and ^{64}Cu into microspheres. This approach increased Cerenkov signal intensity in tissue phantoms compared with ^{64}Cu alone, due to the better penetrating redshifted spectrum of CRET and SCIFI and also to some effect of the higher n of the oil within the liposome. However, this phenomenon is concentration dependent, and therefore such increases are unlikely *in vivo* due to a much greater distance between the particles compared with a well plate. In addition, the particles had a 1,500 nm diameter, which would preclude most *in vivo* uses, as would injection of wintergreen oil into patients.

As a further step in refinement, radionuclides can also be incorporated directly into the crystalline structure of a nanoparticle. This can be done by methods such as addition of the desired radiotracer during nanoparticle synthesis or ionic exchange, where a radionuclide exchanges with its cold elemental counterpart[36]. An interesting alternative to this radiolabelling route is using a cyclotron beam for intrinsically radiolabelled nanoparticles[47]. However, due to the necessity of an on-site cyclotron, this route is impractical for most locations. An advantage to this intrinsic radiolabelling route is increased stability, especially *in vivo*, along with the possibility of very high specific activity concentrated within the nanoparticles, resulting in a high CL flux. One potential downside of this approach is the possibility of crystalline mismatch if the radioactive element greatly differs from the element that makes up the rest of the particle's lattice, resulting in radionuclide detachment. Examples of radiodoped lattices are rare-earth fluorine nanocrystals[48] as well as gold[49], iron oxide[40] and copper nanoparticles[50]. Avoiding issues of crystalline mismatch, fluorescent gold nanoparticles have been doped with ^{198}Au, allowing both nuclear and optical imaging with the same nanoparticle[51]. ^{198}Au is a single-photon emission computed tomography (SPECT) tracer that also emits a high-energy β^- particle, allowing for both whole-body imaging and therapeutic use. Due to its relatively high energy (β_{max} = 0.961 MeV), the β^- emission also results in appreciable CL. By incorporating ^{198}Au directly into the gold lattice, the radionuclide remains stable *in vivo*; in addition, the incorporation did not require surface modification (as when a chelator is used). However, the authors did not use the CL

as an internal excitation source. A similar radiolabelling technique was utilized to radiolabel gold nanospheres, rods, disks and cages with ^{198}Au. By incorporating the radionuclide into the lattice, each nanostructure's biodistribution could be evaluated *in vivo*, using CLI and SPECT imaging without surface modification. The pharmacokinetics as well as the tumour distribution of the variously shaped gold nanoparticles were evaluated using CLI and showed heterogeneous regional uptake in the tumour dependent on the particle shape (Fig. 5a,b)[49].

Copper-64 is another metal that is often used for lattice doping due to its amenable half-life ($t_{1/2}$ = 12.7 h) and facile lattice incorporation. Gold nanoclusters were labelled with ^{64}Cu through reduction with hydrazine and incorporation into the nanoparticle lattice rather than the protein coating of these clusters. These gold nanoclusters were stable *in vivo* and allowed both PET and CLI out to 24 h post-injection[52]. In another demonstration of CL with QDs, ^{64}Cu was doped into CdSe–ZnS QDs via ion exchange for PET and SCIFI[53], and has also been directly incorporated into CuInS–ZnS QDs, alleviating any potential crystalline mismatch issues[54]. When surface-coated with polyethylene glycol (PEGylated), the CuInS–ZnS QDs showed optimal radiochemical stability *in vivo* and tumour uptake as high as 10.8% injected dose per gram (Fig. 5c–e). While QDs are a popular choice for SCIFI, relatively few studies use lattice doping with radioactivity for labelling. This is likely due to crystalline mismatching, the necessity of surface modification before *in vivo* use and increased radioactive waste using this method. However, CL nanocrystals would be attractive for clinical use due to their high stability and multimodal nature. By developing methods that eliminate post-radiolabelling modification and thereby making good manufacturing practice feasible, CL nanocrystals have a greater chance to reach the clinic, for example, for facile imaging and detection of sentinel lymph nodes in oncologic surgery. Currently, suitable Cerenkov imaging systems are being explored.

Cerenkov-activatable probes and therapies

While shifting the CL spectrum with nanoparticles provides distinct advantages for *in vivo* imaging, the systems described thus far emit signal regardless of their biological context, that is, they are 'always on'. This is the typical state of radiotracers that emit a high-energy decay signal, that is, the 511 keV annihilation photons from positron annihilation, which cannot be modulated easily. Therefore, activatable 'smart' imaging systems using radiotracers were until recently not possible. However, CL offers the unique opportunity to modulate a radioactive decay signal for the first time. By using appropriately designed nanosensors, modulation of the signal through spectral shifting, absorption or direct photoactivation by CL has become possible, leading to a new class of smart, functional nanoparticles.

In a first proof of concept, CL was used to photoactivate caged luciferin (though it is not a nanoparticle) in a breast cancer animal model expressing luciferase[55]. Luciferase, an enzyme, is often transfected into cells, allowing *in vivo* bioluminescence imaging when injected luciferin is converted to oxyluciferin (and light) by luciferase. Here, CL was required to activate the caged luciferin, demonstrating the advantage of internal excitation of a fluorophore in the interior of a tumour where external light sources may not reach. A

bioluminescence signal was only obtained when CL was present. In another activatable system, a nanosensor modulated CL through quenching via a direct energy transfer between a radiometal and QDs[32]. A distance-dependent quenching effect was shown using varying lengths of DNA conjugated with the copper chelator DOTA. The copper–DNA constructs were shown to quench QDs via either a photoinduced electron-transfer process or energy transfer (or a combination of both) that was dependent on the distance. This has allowed activatable imaging agents where displacement of a DNA strand with the Cerenkov emitter bound to a QD could ‘turn on QD emission.

While Cerenkov light is typically used to excite fluorophores, it was demonstrated that the absorption curve of iron oxide nanoparticles overlays the CL spectrum almost perfectly, which makes the nanoparticles ideally suited to absorb the Cerenkov emission, decrease signal and result in negative CL contrast[56]. Thorek *et al.* demonstrated this concept *in vivo* with nanoparticles targeting the human somatostatin receptor subtype-2 ($hSSTr_2$). Dual tumour-bearing mice with one tumour expressing $hSSTr_2$ and one tumour not expressing the biomarker were first injected with $hSSTr_2$-targeted nanoparticles. This was followed by injection of [^{18}F]-FDG with PET and CL imaging. $hSSTr_2$-positive tumours had a decrease in CL due to nanoparticle quenching, whereas tumours absent of $hSSTr_2$ showed no change in CL. Nanoparticles therefore provide, for the first time, the opportunity to modulate a radiation-based decay signal in different ways through its Cerenkov signature. Using this technique, multiparameter non-invasive tumour marker imaging is possible.

In another activatable system, nanoparticles were utilized to create a Cerenkov-excited smart nanoconstruct that was switched on by enzymatic activity *in vivo*. Here, gold nanoparticles were used to quench a fluorochrome (FAM) through resonance transfer. The fluorochrome’s Cerenkov-mediated excitation only occurred after its enzyme-mediated release from the gold nanoparticle, thus recovering the Cerenkov-excited fluorescence and indicating enzymatic activity *in vivo* (Fig. 6a). Through this method, matrix metallopeptidase-2 enzyme activity, implicated in tumour aggressiveness, was not only imaged *in vivo* with lower background compared with traditional optical techniques but was also quantifiable directly, using a combination of optical and PET imaging (Fig. 6b–d)[27]. The quantitative PET signal provides an internal standard for Cerenkov imaging that allows the determination of the expected light output.

The use of a common diagnostic clinical radiotracer (for example, [^{18}F]-FDG) with nanoparticles could allow therapeutic opportunities during routine PET imaging. Here, CL can be combined with photon-activatable therapeutic entities. Similar to internal excitation of fluorescent agents, CL has recently been used together with nanoparticles to overcome the current depth limitation of light-activated therapy. Kotagiri *et al.* combined photodynamic therapy (PDT) agent–nanoparticle constructs with positron emitters for Cerenkov radiation-induced therapy, or CRIT. CL from [^{18}F]-FDG activated radical formation from titanium dioxide nanoparticles doped with an additional photosensitizer, titanocene, in both aerobic and anaerobic environments (Fig. 6e – g). The nanoparticles, termed nanophotosensitizers, were targeted to tumours via transferrin attached to the surface, and the PDT from the combination of titanium dioxide and [^{18}F]-FDG showed a significant survival benefit compared with either of the agents alone. This work utilized the internal CL to photoactivate

the nanoconstruct for oxidation-based therapy, for the first time liberating photodynamic therapy from the need of an external excitation source, similar to the internal excitation of fluorochromes[57], with similar work using ^{89}Zr-nanoconstruct combinations also demonstrating therapeutic efficacy[58]. This approach is attractive due to the potential utilization of photodynamic therapeutics with clinical radiotracers already in routine use. This could allow expansion of photodynamic therapy to multimetastatic disease where a targeted radiotracer provides the internal excitation for the photoactivatable therapeutic agent. Another interesting avenue shown in a preliminary study is combining external beam radiation with PDT-active nanoparticles for an enhanced therapeutic effect[59]. As the total light fluence of external beam therapy (mJ cm^{-2}) is much greater than that from radionuclides (nJ cm^{-2}), this strategy has great potential; however, the difference in PDT excitation from radionuclides (lower photon flux over longer time periods dependent on the radionuclide) versus external beam (shorter, high-intensity PDT excitation) need to be further explored[60].

Metamaterials and photonic crystals

While *in vivo* applications abound for Cerenkov imaging and therapy, theoretical and nanolithography advances in the physics and materials science fields have opened another exciting avenue for application of the Cerenkov effect through the use of metamaterials. Taking n as the product of permittivity and permeability, Veselago showed theoretically that for a material with negative n, the Cerenkov cone angle will be obtuse and face backwards (Fig. 7a)[61,62]. At the time in 1968, Veselago's theory could not be tested as no such material or device existed[63], but at the turn of the twenty-first century, advances in lithography provided access to these repetitively structured materials with a negative n (Fig. 7b–e)[64,65], showing potential applications in subdiffraction-limited imaging[66], transformation optics[67], light focusing[68] and even trapping of light[69]. As lithography techniques advanced, metamaterials operating in the microwave range could be tuned to the optical region of the electromagnetic spectrum[70–72]. Finally having NIMs in the optical range, Veselago's predictions could be confirmed experimentally, showing the inverted cone of light, first indirectly through the use of waveguides[73] then directly using a phased electromagnetic dipole array[74]. Applications of NIMs in the context of nanoparticles and CL overcame existing boundaries: from improving the sensitivity and linearity for Cerenkov detectors affected by cone angle saturation[75] to generating CL without an energy threshold as required in the Frank–Tamm formula.

Vesalago's theory was additionally verified by Lu with the mathematical solution for CL in a NIM that also showed that the power propagation is not exactly opposite to the phase propagation when energy absorption by the material occurs[76]. More recent theoretical work involving CL showed that one-dimensional nanoarrays of metal slits could produce Cerenkov wakes vertically in nanoslits. As electrons pass across the surface of the metamaterial, a Cerenkov-like cone is produced in the slits without an energy threshold as required by the Frank–Tamm equation[77]. Use of nanometamaterials like these to overcome CL thresholds could improve the performance of free-electron lasers and wakefield accelerators through the removal of thermal issues and dielectric breakdown commonly found in other materials. Recently, the Cerenkov mechanism with graphene was also shown

to not be confined by the classical Frank–Tamm limit[78]. The simple flow of charge through graphene revealed the generation of graphene plasmons through a two-dimensional Cerenkov emission process. The high Cerenkov emission rate over a wide range of energies was attributed to the low phase velocity and high confinement of the graphene plasmons. These findings intriguingly could explain the higher-than-expected luminescence of graphene, though short hot carrier lifetimes and scattering so far keep near perfect CL conversion efficiency from occurring. While graphene is not in itself a metamaterial, these findings have wide implications in the accuracy of black-body radiation measurements in heterostructures and other condensed-matter systems.

Another important benefit of metamaterials for Cerenkov generation is the amplification of CL. Cerenkov radiation formed in a metamaterial of periodic arrays of parallel metallic nanorods showed increased emission by an order of magnitude, along with producing CL without the Cerenkov particle velocity threshold. Increased Cerenkov emission occurred through a rise in stopping power (that is, the average energy loss of the particles per unit of path length) by two orders of magnitude compared with water[79]. This simulated nanowire was considered a perfect conductor with no electromagnetic energy dissipated to the nanowire, thus allowing electronic oscillations to exist at any velocity and removing the Cerenkov threshold. Furthermore, more nanowires lead to more radiative oscillations, and thus more Cerenkov emission. This absence of an energy threshold was also separately demonstrated in the simulation of a metamaterial with a series of slits in a metal[80]. Building on the metal slit design, an additional periodicity was introduced to the metamaterial (Fig. 7d–e), which revealed a magnitude increase in CL intensity of several orders[81]. Through deliberate periodic design, metamaterials can disobey CL generation requirements previously thought as fundamental phenomena properties.

Beyond amplification, steering light by metamaterials is also of interest, allowing photons to be channelled instead of simply scattered. This CL steering was first shown with colloidal silver nanocubes deposited onto a thin gold film, where tuning the size and spacing of the nanocubes on the film changes the permittivity and permeability without changing the dielectric environment. This method is highly advantageous as the metamaterial assembly relies on colloidal properties. The interface between the Au film and Ag nanocubes exhibited extreme light confinement to optical cavities with dimensions less than 200 nm, however >98% of the signal is absorbed at the desired wavelength, representing an area for future optimization[82]. Genevet *et al.* alternatively used a one-dimensional metamaterial etched with subwavelength rotated apertures to produce a metamaterial designed to steer Cerenkov light[83]. Steering or trapping of Cerenkov light represents an exciting area for CL as optical paths could be built from metamaterials to parse wavefunctions for diagnostic and optical computing purposes.

Another type of nanomaterial demonstrating CL modulation are photonic crystals, which contain periodic differing dielectric structures and a photonic bandgap. A photonic bandgap represents the range of frequencies within a material where photons cannot propagate. While photonic structures have been known since the nineteenth century, the first photonic crystals were described in 1987[84], with the best-known natural example being opal. Photons can interact with photonic crystals in ways analogous to electrons travelling through an ionic

lattice, and allow modulation of CL via mechanisms different from NIMs[85]. The introduction of point or line defects into a crystal adjusts the photonic bandgap and alters the flow of light through the crystal. Through periodic phonon (uniform oscillation of atoms in a lattice at one frequency) modulation, exclusion of optical modes in desired frequencies can be achieved. Electrons that do not meet the traditional Cerenkov threshold were shown to still result in CL through momentum transfer followed by phonon creation[86]. Going further, photonic crystals propagate light (such as CL) differently than traditional mediums, where light travels as a Bloch wave instead of a traditional (sinusoidal/oscillating) wave[87]. Within the photonic crystal, increasing the velocity of the charged particle from $0.1c$ where no Cerenkov cone forms, to between $0.2c$ and $0.4c$ results in a forward pointing cone, yet the radiation is collimated in the backwards direction (Fig. 7f). While this resembles the predicted behaviour of a NIM, the photonic crystal is a positive-index material based on the wavevector. Potential applications of this selective cone formation lie in velocity-sensitive Cerenkov detectors and CL generation at selectable frequencies. Of potential use in particle detectors, it was recently shown that photonic crystals can slow down the propagation of CL appreciably and further control the behaviour of CL[88,89]. In both metamaterial and photonic crystal examples, CL can be modulated to disobey theories that were assumed fundamental to light generation. By exploiting how light propagates within these mediums, CL is a powerful tool in determining material composition. Conversely, selecting the correct material allows the identification of highly charged particles, extracting information about Cerenkov radiation not possible with conventional structures. While examples mainly benefit detectors used in physics, translation of these materials into medical devices and the patient have yet to be determined.

Conclusions and outlook

After nearly a century since its discovery, interest in the Cerenkov effect has now expanded into both basic and applied nanosciences, resulting in a wealth of new applications and phenomena to be explored. The advantages of combining nanotechnology and CL have already been demonstrated in preclinical models. One possible avenue into the clinical arena is utilizing nano-enhanced CL for surgical guidance during resection of tumours and draining sentinel lymph nodes[90]. Radiolabelled nano- and microparticles are used clinically for sentinel lymph node imaging, with ^{99m}Tc colloids in widespread clinical use. As ^{99m}Tc colloids do not emit CL, the development of a CL-emitting nanoparticle for routine clinical use would expand lymph node imaging from nuclear to multimodal (that is, nuclear and optical), aiding in surgical resection. With the removal of overlaying tissue, scattering and absorption of CL is reduced. At the same time, deeper lesions can still be detected with the aid of handheld probes detecting radioactivity. CL also allows superior surface resolution compared with nuclear imaging, which is advantageous for detection of tumour margins[91] and could be significantly improved using nanoparticles.

Recently, the possibility of utilizing CL with nanoparticles and PDT agents was realized. As radiotracers are typically injected for diagnostic imaging or radiotherapy; and brachytherapy is used to treat certain cancers such as prostate cancer, it is feasible that the addition of a PDT nanoagent for adjuvant therapy would be therapeutically beneficial. External beam PDT combinations are also promising for rapid clinical translation, as CLI of external beam

therapy has already been used clinically to monitor positioning and dosimetry[92–94]. One underdeveloped area is investigating the various excitation mechanisms of the PDT nanoagents, as theoretical work reveals the photon flux from CL is too low to entirely account for the observed PDT responses[60].

Yet another future application of CL is in the burgeoning field of optogenetics. Here, visible light (typically blue) activates light-sensitive ion channels at specific anatomical areas (commonly neurons). Currently activated through fibre optics or optoelectronics[95], the possibility of using CL from radiotracers to activate precise anatomical locations could allow non-invasive, targeted optogenetics, with precise spectrum emissions possible through combination with nanoparticles to enhance the Cerenkov signal significantly. Indeed, nanoparticles have recently been used in optogenetics[96], but combination with CL has yet to be achieved.

In materials science, the experimental demonstration of double-negative metamaterials and increased control of the properties of nanoparticles has allowed for new Cerenkov applications beyond particle physics and beyond the relationships described in the Frank–Tamm equation. Here, metamaterial nanostructures offer the possibility of guiding electromagnetic waves. An interesting investigation would be combining metamaterials with a high refractive index in the optical window with Cerenkov radiation[97]. Nanoparticles assembled to form metamaterials would allow novel and miniaturized radiation detectors, where radioactivity can be detected using optical signatures from any radiotracer, even those that produce particles with energy under the Cerenkov threshold. New opportunities for Cerenkov applications appear as nanoscience and materials research advances, with some experimental results long-postulated and others surprising the field.

Acknowledgments

We acknowledge funding from the National Institutes of Health (NIH) R01EB014944 and R01CA183953 and P30 CA08748, in addition to National Science Foundation (NSF) IGERT traineeship DGS 0965983.

References

1. Heaviside O. The electromagnetic effect of a moving charge. The Electrician. 1888; 2:83–84.
2. Cerenkov P. Visible light from pure liquids under the impact of gamma-rays. C. R. Acad. Sci. Urss. 1934; 3:451–457.
3. Bolotovskii BM. Vavilov-Cherenkov radiation: its discovery and application. Phys-Usp. 2009; 52:1099–1110.
4. Čerenkov PA. Visible radiation produced by electrons moving in a medium with velocities exceeding that of light. Phys. Rev. 1937; 52:378–379.
5. Frank I, Tamm I. Coherent visible radiation of fast electrons passing through matter. C. R. Acad. Sci. Urss. 1937; 14:109–114.
6. Ginzburg VL. The quantum theory of radiation of an electron uniformly moving in a medium. J. Phys. USSR. 1940; 2:441–452.
7. Choppin, G., Liljenzin, J-O., Rydberg, J., Ekberg, C. Radiochemistry and Nuclear Chemistry. 4. Academic Press; 2013.
8. Kaminer I, et al. Quantum Cerenkov radiation: spectral cutoffs and the role of spin and orbital angular momentum. Phys. Rev. X. 2015; 6:011006.
9. Kobzev AP. The mechanism of Vavilov-Cherenkov radiation. Phys. Part. Nuclei. 2010; 41:452–470.

10. Kobzev AP. On the radiation mechanism of a uniformly moving charge. Phys. Part. Nuclei. 2014; 45:628–653.
11. Thorek D, et al. Cerenkov imaging — a new modality for molecular imaging. Am. J. Nucl. Med. Mol. Imaging. 2012; 2:163–173. [PubMed: 23133811]
12. Gill RK, Mitchell GS, Cherry SR. Computed Cerenkov luminescence yields for radionuclides used in biology and medicine. Phys. Med. Biol. 2015; 60:4263–4280. [PubMed: 25973972]
13. Krizan P. Recent progress in Cerenkov counters. IEEE Trans. Nucl. Sci. 2001; 48:941–949.
14. Abeysekara AU, et al. Sensitivity of the high altitude water Cherenkov detector to sources of multi-TeV gamma rays. Astropart. Phys. 2013; 50–52:26–32.
15. Chamberlain O, Segre E, Wiegand C, Ypsilantis T. Observation of antiprotons. Phys. Rev. 1955; 100:947–950.
16. Aubert JJ, et al. Experimental observation of a heavy particle. J. Phys. Rev. Lett. 1974; 33:1404–1406.
17. Augustin JE, et al. Discovery of a narrow resonance in e^+e^- annihilation. Phys. Rev. Lett. 1974; 33:1406–1408.
18. Robertson R, et al. Optical imaging of Cerenkov light generation from positron-emitting radiotracers. Phys. Med. Biol. 2009; 54:N355–N365. The first preclinical demonstration of *in vivo* CLI using injected radiotracers. [PubMed: 19636082]
19. Beattie BJ, et al. Quantitative modeling of Cerenkov light production efficiency from medical radionuclides. PloS ONE. 2012; 7:e31402. [PubMed: 22363636]
20. Boschi F, et al. *In vivo* (18)F-FDG tumour uptake measurements in small animals using Cerenkov radiation. Eur. J. Nucl. Med. Mol. Imaging. 2011; 38:120–127. [PubMed: 20882278]
21. Mitchell GS, Gill RK, Boucher DL, Li C, Cherry SR. *In vivo* Cerenkov luminescence imaging: a new tool for molecular imaging. Phil. Trans. R. Soc. A. 2011; 369:4605–4619. [PubMed: 22006909]
22. Lohrmann C, et al. Cerenkov luminescence imaging for radiation dose calculation of a ^{90}Y-labeled gastrin-releasing peptide receptor antagonist. J. Nucl. Med. 2015; 56:805–811. [PubMed: 25840974]
23. Pandya DN, et al. Preliminary therapy evaluation of ^{225}Ac-DOTA-c(RGDyK) demonstrates that Cerenkov radiation derived from ^{225}Ac daughter decay can be detected by optical imaging for *in vivo* tumor visualization. Theranostics. 2016; 6:698–709. [PubMed: 27022417]
24. Spinelli AE, et al. First human Cerenkography. J. Biomed. Opt. 2013; 18:20502. [PubMed: 23334715]
25. Thorek DL, Riedl CC, Grimm J. Clinical Cerenkov luminescence imaging of ^{18}F-FDG. J. Nucl. Med. 2014; 55:95–98. [PubMed: 24078721]
26. Chin PT, et al. Optical imaging as an expansion of nuclear medicine: Cerenkov-based luminescence vs fluorescence-based luminescence. Eur. J. Nucl. Med. Mol. Imaging. 2013; 40:1283–1291. [PubMed: 23674205]
27. Thorek DL, Ogirala A, Beattie BJ, Grimm J. Quantitative imaging of disease signatures through radioactive decay signal conversion. Nat. Med. 2013; 19:1345–1350. A paper that shows how CL combinations with nanoparticle allows *in vivo* activatable molecular imaging. [PubMed: 24013701]
28. Dothager RS, Goiffon RJ, Jackson E, Harpstrite S, Piwnica-Worms D. Cerenkov radiation energy transfer (CRET) imaging: a novel method for optical imaging of PET isotopes in biological systems. PloS ONE. 2010; 5:e13300. A paper showing how combining photoluminescent nanoparticles with CL allows deeper optical imaging depth. [PubMed: 20949021]
29. Liu H, et al. Radiation-luminescence-excited quantum dots for *in vivo* multiplexed optical imaging. Small. 2010; 6:1087–1091. [PubMed: 20473988]
30. Hu Z, et al. *In vivo* nanoparticle-mediated radiopharmaceutical-excited fluorescence molecular imaging. Nat. Commun. 2015; 6:7560. [PubMed: 26123615]
31. Ma X, et al. Enhancement of Cerenkov luminescence imaging by dual excitation of Er^{3+}, Yb^{3+}-doped rare-earth microparticles. PloS ONE. 2013; 8:e77926. [PubMed: 24205030]

32. Kotagiri N, Niedzwiedzki DM, Ohara K, Achilefu S. Activatable probes based on distance-dependent luminescence associated with Cerenkov radiation. Angew. Chem. Int. Ed. 2013; 52:7756–7760.
33. Kim J, et al. Vivid tumor imaging utilizing liposome-carried bimodal radiotracer. ACS Med. Chem. Lett. 2014; 5:390–394. [PubMed: 24900846]
34. Perez-Medina C, et al. A modular labeling strategy for *in vivo* PET and near-infrared fluorescence imaging of nanoparticle tumor targeting. J. Nucl. Med. 2014; 55:1706–1711. [PubMed: 25060196]
35. Rieffel J, et al. Hexamodal imaging with porphyrin-phospholipid-coated upconversion nanoparticles. Adv. Mater. 2015; 27:1785–1790. [PubMed: 25640213]
36. Goel S, Chen F, Ehlerding EB, Cai W. Intrinsically radiolabeled nanoparticles: an emerging paradigm. Small. 2014; 10:3825–3830. A review on advances in radiolabeling nanoparticles for biomedical applications without using chelators or prosthetic groups. [PubMed: 24978934]
37. Shaffer TM, et al. Silica nanoparticles as substrates for chelator-free labeling of oxophilic radioisotopes. Nano Lett. 2015; 15:864–868. [PubMed: 25559467]
38. Chen F, et al. *In vivo* integrity and biological fate of chelator-free zirconium-89-labeled mesoporous silica nanoparticles. ACS Nano. 2015; 9:7950–7959. [PubMed: 26213260]
39. Shaffer TM. Stable radiolabeling of sulfur-functionalized silica nanoparticles with copper-64. Nano Lett. 2016; 16:5601–5604. [PubMed: 27464258]
40. Boros E, Bowen AM, Josephson L, Vasdev N, Holland JP. Chelate-free metal ion binding and heat-induced radiolabeling of iron oxide nanoparticles. Chem. Sci. 2015; 6:225–236. [PubMed: 28553472]
41. Madru R, et al. ^{68}Ga-labeled superparamagnetic iron oxide nanoparticles (SPIONs) for multi-modality PET/MR/Cherenkov luminescence imaging of sentinel lymph nodes. Am. J. Nucl. Med. Mol. Imaging. 2013; 4:60–69. [PubMed: 24380046]
42. Lee SB, et al. Radionuclide-embedded gold nanoparticles for enhanced dendritic cell-based cancer immunotherapy, sensitive and quantitative tracking of dendritic cells with PET and Cerenkov luminescence. NPG Asia Mater. 2016; 8:e281.
43. Lee SB, et al. Combined positron emission tomography and Cerenkov luminescence imaging of sentinel lymph nodes using PEGylated radionuclide-embedded gold nanoparticles. Small. 2016; 12:4894–4901. [PubMed: 27439987]
44. Karn PR, Cho W, Hwang SJ. Liposomal drug products and recent advances in the synthesis of supercritical fluid-mediated liposomes. Nanomedicine. 2013; 8:1529–1548. [PubMed: 23987112]
45. Black KC, et al. *In vivo* fate tracking of degradable nanoparticles for lung gene transfer using PET and Cerenkov imaging. Biomaterials. 2016; 98:53–63. [PubMed: 27179433]
46. Li J, et al. Enhancement and wavelength-shifted emission of Cerenkov luminescence using multifunctional microspheres. Phys. Med. Biol. 2015; 60:727–739. [PubMed: 25555157]
47. Gibson N, et al. Radiolabelling of engineered nanoparticles for *in vitro* and *in vivo* tracing applications using cyclotron accelerators. Arch. Toxicol. 2011; 85:751–773. [PubMed: 21479952]
48. Paik T, et al. Shape-controlled synthesis of isotopic yttrium-90-labeled rare earth fluoride nanocrystals for multimodal imaging. ACS Nano. 2015; 9:8718–8728. [PubMed: 26257288]
49. Black KC, et al. Radioactive ^{198}Au-doped nanostructures with different shapes for *in vivo* analyses of their biodistribution, tumor uptake, and intratumoral distribution. ACS Nano. 2014; 8:4385–4394. [PubMed: 24766522]
50. Zhao Y, et al. Copper-64-alloyed gold nanoparticles for cancer imaging: improved radiolabel stability and diagnostic accuracy. Angew. Chem. Int. Ed. 2014; 53:156–159.
51. Zhou C, et al. Near-infrared emitting radioactive gold nanoparticles with molecular pharmacokinetics. Angew. Chem. Int. Ed. 2012; 51:10118–10122.
52. Hu H, et al. PET and NIR optical imaging using self-illuminating ^{64}Cu-doped chelator-free gold nanoclusters. Biomaterials. 2014; 35:9868–9876. [PubMed: 25224367]
53. Sun X, et al. Self-illuminating ^{64}Cu-doped CdSe/ZnS nanocrystals for *in vivo* tumor imaging. J. Am. Chem. Soc. 2014; 136:1706–1709. [PubMed: 24401138]

54. Guo W, et al. Intrinsically radioactive [^{64}Cu]CuInS/ZnS quantum dots for PET and optical imaging: improved radiochemical stability and controllable Cerenkov luminescence. ACS Nano. 2015; 9:488–495. [PubMed: 25549258]
55. Ran C, Zhang Z, Hooker J, Moore A. *In vivo* photoactivation without “light”: use of Cherenkov radiation to overcome the penetration limit of light. Mol. Imaging Biol. 2012; 14:156–162. [PubMed: 21538154]
56. Thorek DL, Das S, Grimm J. Molecular imaging using nanoparticle quenchers of Cerenkov luminescence. Small. 2014; 10:3729–3734. A demonstration of combining CL-absorbing iron oxide nanoparticles with radiotracers for molecular imaging. [PubMed: 24861843]
57. Kotagiri N, Sudlow GP, Akers WJ, Achilefu S. Breaking the depth dependency of phototherapy with Cerenkov radiation and low-radiance-responsive nanophotosensitizers. Nat. Nanotech. 2015; 10:370–379. A demonstration on combining CL with photodynamic therapeutic agents for oncology.
58. Kamkaew A, et al. Cerenkov radiation induced photodynamic therapy using chlorin e6-loaded hollow mesoporous silica nanoparticles. ACS Appl. Mater. Interfaces. 2016; 8:26630–26637. [PubMed: 27657487]
59. Ouyang Z, Liu B, Yasmin-Karim S, Sajo E, Ngwa W. Nanoparticle-aided external beam radiotherapy leveraging the Cerenkov effect. Phys. Med. 2016; 32:944–947. [PubMed: 27397906]
60. Glaser AK, Zhang R, Andreozzi JM, Gladstone DJ, Pogue BW. Cherenkov radiation fluence estimates in tissue for molecular imaging and therapy applications. Phys. Med. Biol. 2015; 60:6701–6718. A paper calculating photon fluxes from CL with both radiotracers and external beams. [PubMed: 26270125]
61. Chen HS, Chen M. Flipping photons backward: reversed Cherenkov radiation. Mater. Today. 2011; 14:34–41.
62. Soukoulis CM, Wegener M. Past achievements and future challenges in the development of three-dimensional photonic metamaterials. Nat. Photon. 2011; 5:523–530.
63. Veselago VG. The electrodynamics of substances with simultaneously negative values of ε and μ. Sov. Phys. Uspekhi. 1968; 10:509–514.
64. Pendry JB, Holden AJ, Stewart WJ, Youngs I. Extremely low frequency plasmons in metallic mesostructures. Phys Rev Lett. 1996; 76:4773–4776. [PubMed: 10061377]
65. Smith DR, Padilla WJ, Vier DC, Nemat-Nasser SC, Schultz S. Composite medium with simultaneously negative permeability and permittivity. Phys. Rev. Lett. 2000; 84:4184–4187. [PubMed: 10990641]
66. Cortes CL, Newman W, Molesky S, Jacob Z. Quantum nanophotonics using hyperbolic metamaterials. J. Opt. 2012; 14:063001.
67. Landy N, Smith DR. A full-parameter unidirectional metamaterial cloak for microwaves. Nat. Mater. 2013; 12:25–28. [PubMed: 23142840]
68. Pendry JB. Negative refraction makes a perfect lens. Phys. Rev. Lett. 2000; 85:3966–3969. [PubMed: 11041972]
69. Tsakmakidis KL, Boardman AD, Hess O. ‘Trapped rainbow’ storage of light in metamaterials. Nature. 2007; 450:397–401. [PubMed: 18004380]
70. Shalaev VM. Optical negative-index metamaterials. Nat. Photon. 2007; 1:41–48.
71. Soukoulis CM, Linden S, Wegener M. Negative refractive index at optical wavelengths. Science. 2007; 315:47–49. [PubMed: 17204630]
72. Lezec HJ, Dionne JA, Atwater HA. Negative refraction at visible frequencies. Science. 2007; 316:430–432. [PubMed: 17379773]
73. Antipov S, et al. Observation of wakefield generation in left-handed band of metamaterial-loaded waveguide. J. Appl. Phys. 2008; 104:014901.
74. Xi S, et al. Experimental verification of reversed Cherenkov radiation in left-handed metamaterial. Phys. Rev. Lett. 2009; 103:194801. [PubMed: 20365927]
75. Ginis V, Danckaert J, Veretennicoff I, Tassin P. Controlling Cherenkov radiation with transformation-optical metamaterials. Phys. Rev. Lett. 2014; 113:167402. [PubMed: 25361279]

76. Lu J, et al. Cerenkov radiation in materials with negative permittivity and permeability. Opt. Express. 2003; 11:723–734. [PubMed: 19461784]
77. So JK, et al. Cerenkov radiation in metallic metamaterials. Appl. Phys. Lett. 2010; 97:151107.
78. Kaminer I, et al. Efficient plasmonic emission by the quantum Cerenkov effect from hot carriers in graphene. Nat. Commun. 2016; 7:11880. A demonstration that a molecular nanostructure can operate without traditional Cerenkov requirements much like larger nanofabricated devices.
79. Fernandes DE, Maslovski SI, Silveirinha MG. Cherenkov emission in a nanowire material. Phys. Rev. B. 2012; 85:155107.
80. So J-K, et al. Cerenkov radiation in metallic metamaterials. Appl. Phys. Lett. 2010; 97:151107.
81. Bera A, et al. Surface-coupling of Cerenkov radiation from a modified metallic metamaterial slab via Brillouin-band folding. Opt. Express. 2014; 22:3039–3044. [PubMed: 24663594]
82. Rozin MJ, Rosen DA, Dill TJ, Tao AR. Colloidal metasurfaces displaying near-ideal and tunable light absorbance in the infrared. Nat. Commun. 2015; 6:7325. [PubMed: 26099835]
83. Genevet P, et al. Controlled steering of Cherenkov surface plasmon wakes with a one-dimensional metamaterial. Nat. Nanotech. 2015; 10:804–809.
84. Yablonovitch E. Inhibited spontaneous emission in solid-state physics and electronics. Phys. Rev. Lett. 1987; 58:2059–2062. [PubMed: 10034639]
85. Kremers C, Chigrin DN, Kroha J. Theory of Cherenkov radiation in periodic dielectric media: emission spectrum. Phys. Rev. A. 2009; 79:013829.
86. Stevens TE, Wahlstrand JK, Kuhl J, Merlin R. Cherenkov radiation at speeds below the light threshold: phonon-assisted phase matching. Science. 2001; 291:627–630. [PubMed: 11158670]
87. Luo C, Ibanescu M, Johnson SG, Joannopoulos JD. Cerenkov radiation in photonic crystals. Science. 2003; 299:368–371. [PubMed: 12532010]
88. Anishchenko SV, Baryshevsky VG. Cooperative parametric (quasi-Cherenkov) radiation produced by electron bunches in natural or photonic crystals. Nucl. Instrum. Methods B. 2015; 355:76–80.
89. Tao J, Wang QJ, Zhang JJ, Luo Y. Reverse surface-polariton Cherenkov radiation. Sci. Rep. 2016; 6:30704. [PubMed: 27477061]
90. Holland JP, Normand G, Ruggiero A, Lewis JS, Grimm J. Intraoperative imaging of positron emission tomographic radiotracers using Cerenkov luminescence emissions. Mol. Imaging. 2011; 10:177–186. [PubMed: 21496448]
91. Thorek DL, et al. Positron lymphography: multimodal, high-resolution, dynamic mapping and resection of lymph nodes after intradermal injection of ^{18}F-FDG. J. Nucl. Med. 2012; 53:1438–1445. [PubMed: 22872741]
92. Glaser AK, et al. Projection imaging of photon beams by the Cerenkov effect. Med. Phys. 2013; 40:012101. [PubMed: 23298103]
93. Glaser AK, et al. Three-dimensional Cerenkov tomography of energy deposition from ionizing radiation beams. Opt. Lett. 2013; 38:634–636. [PubMed: 23455248]
94. Helo Y, Kacperek A, Rosenberg I, Royle G, Gibson AP. The physics of Cerenkov light production during proton therapy. Phys. Med. Biol. 2014; 59:7107–7123. [PubMed: 25365447]
95. Kim TI, et al. Injectable, cellular-scale optoelectronics with applications for wireless optogenetics. Science. 2013; 340:211–216. [PubMed: 23580530]
96. Wu X, et al. Dye-sensitized core/active shell upconversion nanoparticles for optogenetics and bioimaging applications. ACS Nano. 2016; 10:1060–1066. [PubMed: 26736013]
97. Kothapalli SR, Liu H, Liao JC, Cheng Z, Gambhir SS. Endoscopic imaging of Cerenkov luminescence. Biomed. Opt. Express. 2012; 3:1215–1225. [PubMed: 22741069]
98. Nuclear Structure and Decay Data. National Nuclear Data Center; 2016.

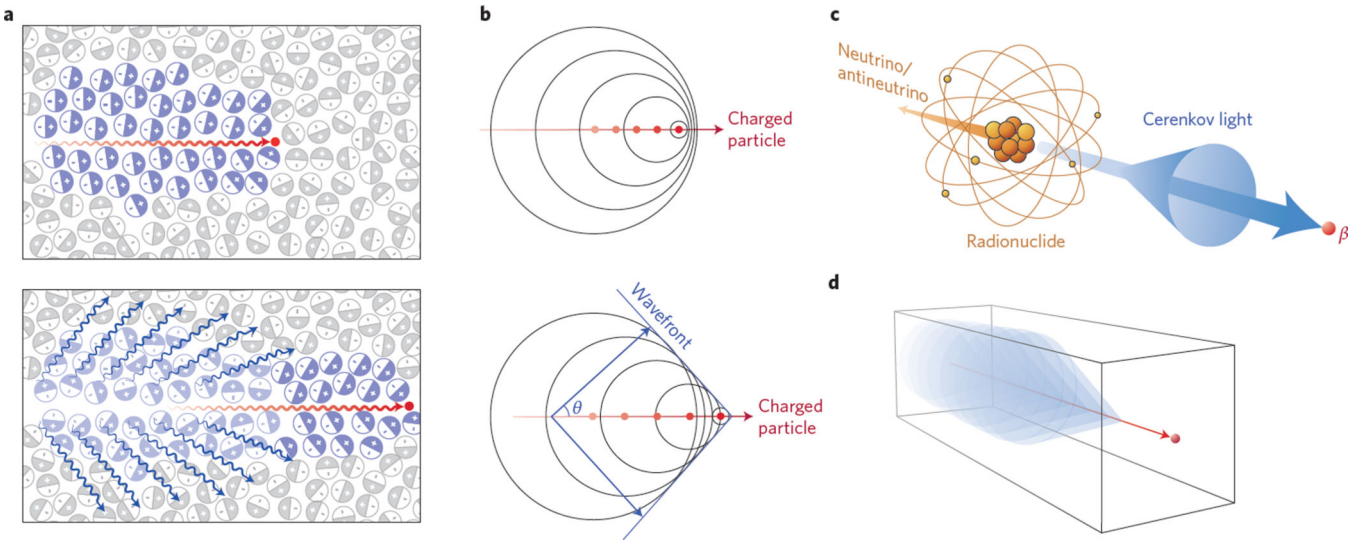

Figure 1. The Cerenkov mechanism for blue-weighted luminescence

a, Top: A charged particle (red dot) travelling faster than light in a medium polarizes the medium. Bottom: As the medium returns to the ground state, blue-weighted light (blue wavy lines) is emitted in a forward direction. **b**, Analogous to a sonic boom, coherent waves are produced through the Cerenkov mechanism, leading to a photonic wavefront. As the particle travels forward (lower panel) the photonic wavefront propagates at a forward angle θ with light being emitted in the direction of travel. **c**, Cerenkov light is emitted (blue cone and arrow) by the medium in which a charged particle travels. Radionuclides that emit β-particles with energies greater than the Cerenkov threshold (261 keV in water) result in CL. **d**, In negative index materials, the cone of Cerenkov light is reversed compared with conventional materials, as in **c**.

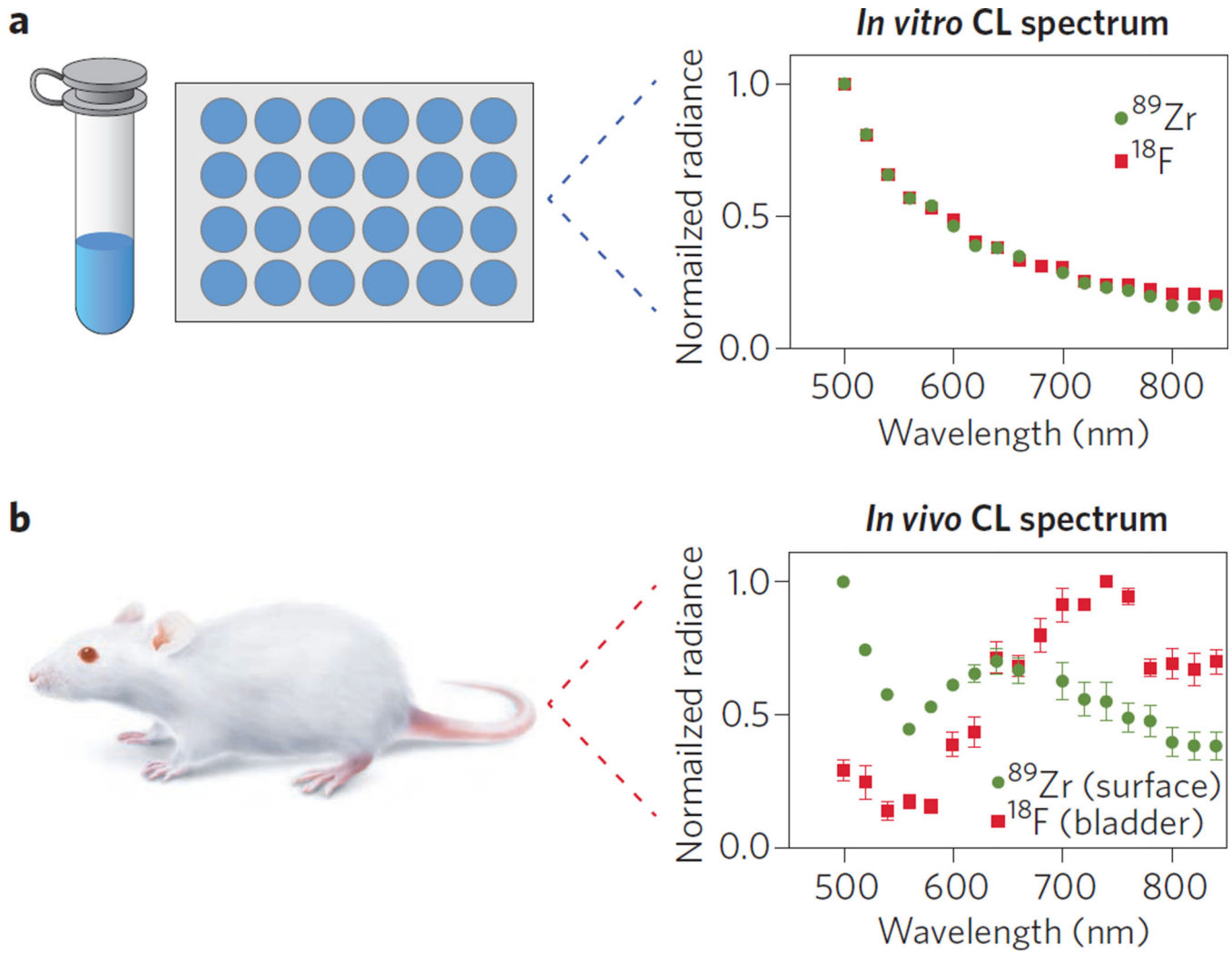

Figure 2. Challenges of *in vivo* imaging of CL, highlighting the utility of photoluminescent nanoparticles

a, *In vitro* systems show the characteristic $1/\lambda^2$ spectrum as expected by the Frank–Tamm equation. Through the use of a calibrated preclinical optical scanner, a quantitative spectrum of CL from 100 μCi (3.7 MBq) of [^{18}F]-FDG (red) or ^{89}Zr (green) is obtained. **b**, When imaging CL *in vivo*, attenuation of higher-frequency photons is seen. Here, the CL spectrum from [^{18}F]-FDG in the bladder of a mouse shows maximum intensities at wavelengths in the red–near-infrared region, whereas ^{89}Zr in a matrigel plug closer to the surface has less attenuation of shorter-wavelength photons. The *in vivo* attenuation of the blue-weighted CL has led to the use of photoluminescent nanoparticles to address this shortcoming. Normalized radiance values (mean with s.d, $n = 4$) are shown.

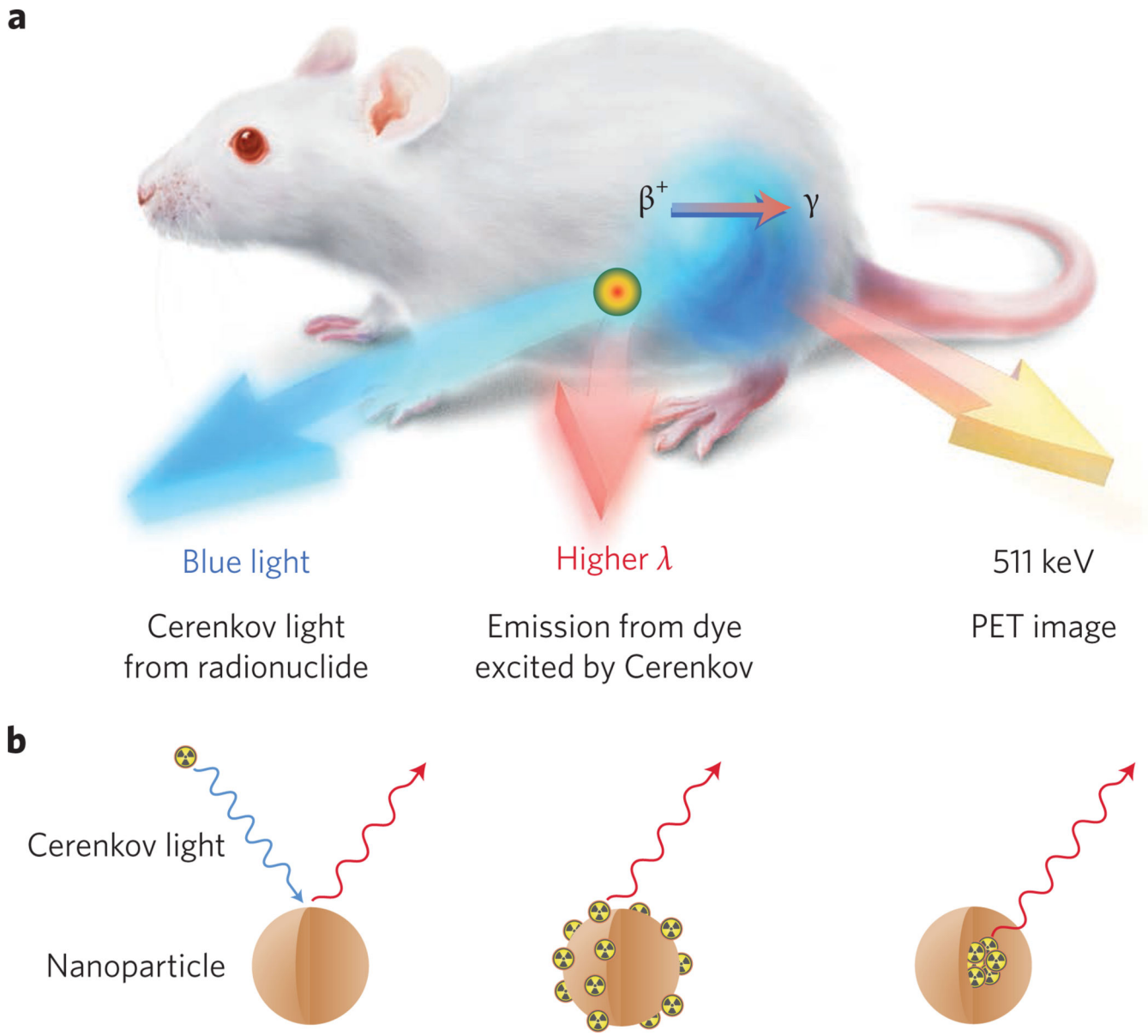

Figure 3. Nanoparticle combinations with CL allow improved *in vivo* imaging

a, The three signals obtained from a CL–fluorescent nanoparticle (for example, QD) system: the blue CL, the red-shifted fluorescence and the PET signal, serving as an internal standard for quantification, make this a unique, truly multimodal quantitative system. High-energy electron–nanoparticle systems result in blue CL and redshifted fluorescence only. **b**, Three types of Cerenkov light–nanoparticle interactions: unbound Cerenkov emitters (left), surface-bound Cerenkov emitters (centre) and intrinsically self-illuminating crystals (right). Unbound Cerenkov emitters offer ease of translation through the possibility of using clinical radiotracers such as [^{18}F]-FDG, but require co-location in space and time *in vivo*. Surface-bound Cerenkov emitters do not have the co-location limitation, but may result in possibly undesired signal from nonspecific distribution of the radiolabelled nanoparticle. Intrinsically self-illuminating particles offer superior *in vivo* stability, but the choice of nanoparticle–

radionuclide system is limited by the possibility of lattice mismatch between the radionuclide and the nanoparticle elements.

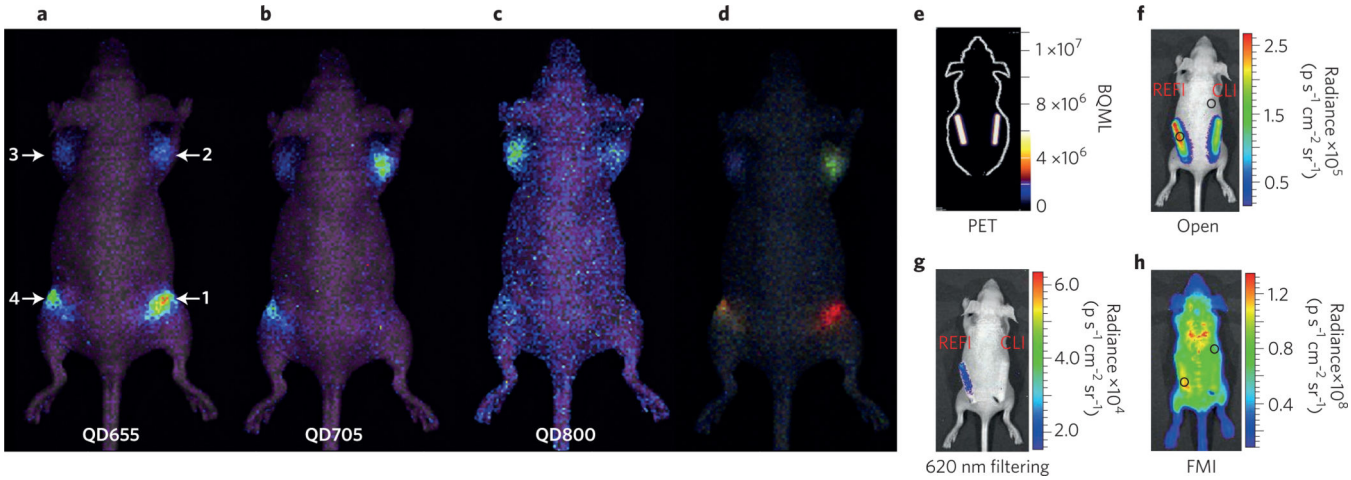

Figure 4. Clinical small-molecule radiotracers and nanoparticles offer ease of clinical translation

a–d, IVIS optical images of QDs exhibiting SCIFI, where CL is shifted from blue light to more tissue-penetrating red light. Injection sites contain: 1, QD655/^{131}I; 2, QD705/^{131}I; 3, QD800/^{131}I; 4, QD655/QD705/QD800/^{131}I. All samples were injected intramuscularly with 0.37 MBq of ^{131}I. **a**, QD655 filter (620–700 nm). **b**, QD705 filter (660–800 nm). **c**, QD 800 filter (760–840 nm). **d**, The spectral unmixed image of the same mouse, showing the different QD locations, represented by different colours. **e–h**, REFI demonstrates superior contrast compared with CLI and fluorescence molecular imaging (FMI). **e**, PET imaging showing equal ^{18}F activity in each phantom. **f,g**, REFI and CLI of europium oxide nanoparticles with ^{18}F show significant differences between no filtering (**f**) and a 620 nm filter (**g**). **h**, FMI of the *in vivo* phantom. Panels reproduced from ref. 29, Wiley (**a–d**) and ref. 30, Macmillan Publishers Ltd (**e–h**).

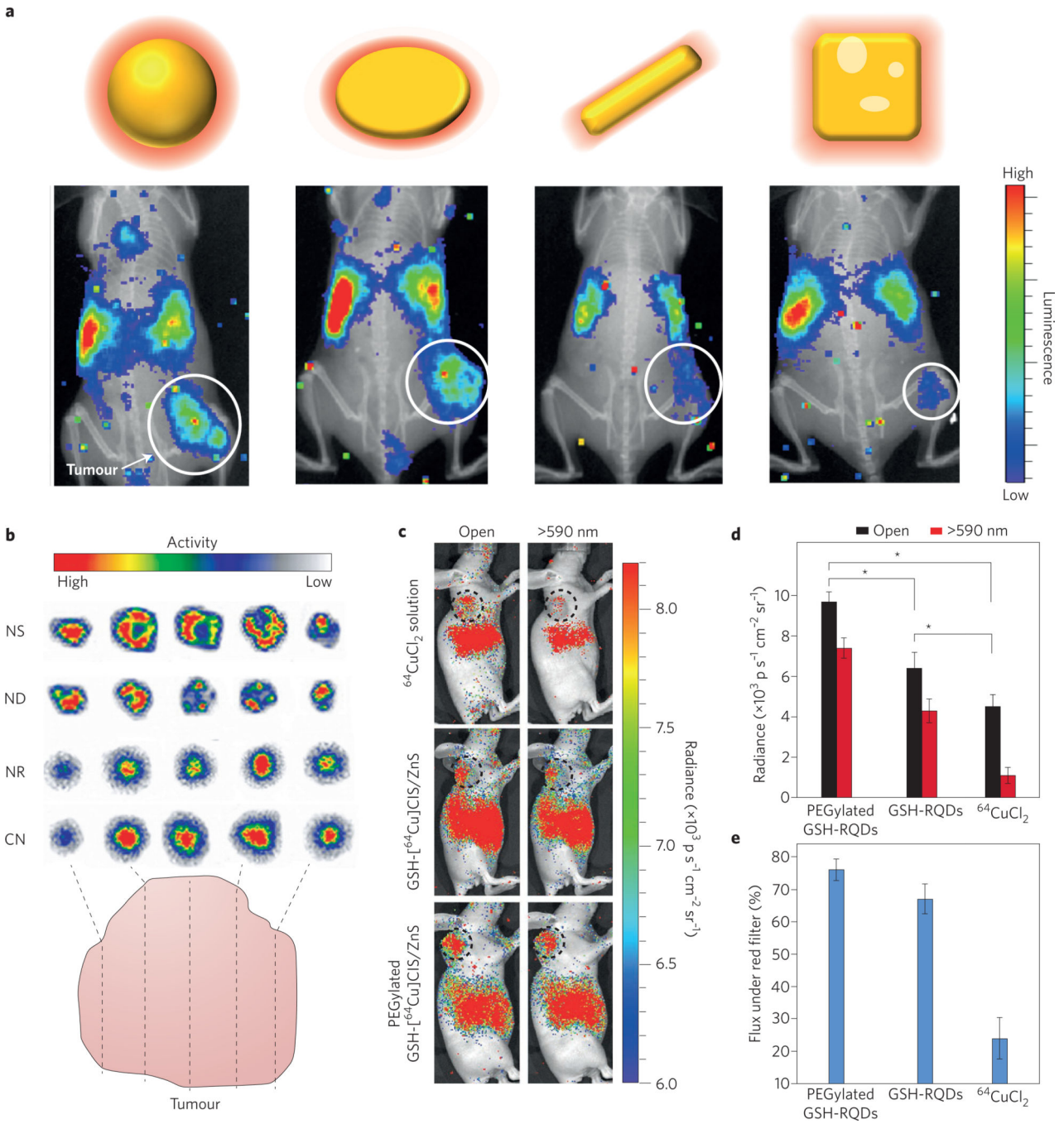

Figure 5. CL emitters can be incorporated into nanoparticles for high specific activity, multimodal probes

a, Different shaped gold nanostructures lead to differential biodistribution and tumour uptake. **b**, Autoradiographic images of tumour slices at 24 h post-injection of ^{198}Au-incorporated gold nanospheres (NS), nanodiscs (ND), nanorods (NR) and cubic nanocages (CN). **c**, CL images of U87MG tumour-bearing mice at 6 h post-injection of 11.1 MBq of $^{64}CuCl_2$, glutathione (GSH)-[^{64}Cu]CIS/ZnS and PEGylated GSH-[^{64}Cu]CIS/ZnS QDs, respectively, obtained with open and red filters (590 nm). The tumour is circled. **d**, Total

photon flux in the corresponding tumour region obtained with open and red filters (*$p <$ 0.05, $n = 3$, s.d. shown). **e**, The percentage of photon flux under a red filter in the total photon flux (*$p < 0.05$, $n = 3$, s.d shown). Panels reproduced from ref. 49, American Chemical Society (**a,b**) and ref. 54, American Chemical Society (**c–e**).

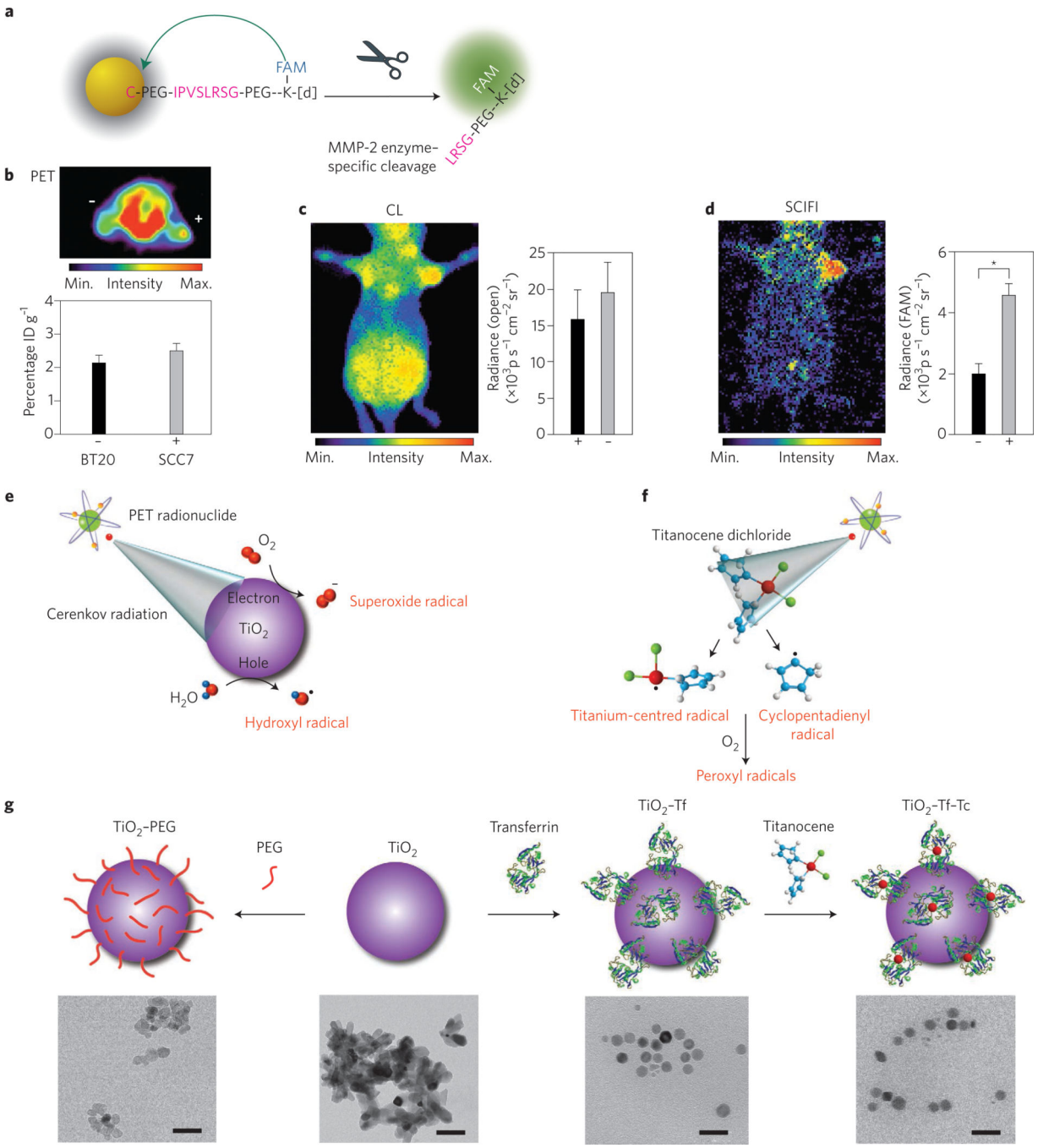

Figure 6. Smart, activatable nanoparticles allow *in vivo* modulation of radioactive signal along with therapeutic opportunities

a–d, CL for activatable imaging using radionuclides ($n = 3$, s.d. shown). **a**, Schematic of an enzyme-activatable SCIFI probe. Fluorescence is quenched when the fluorescein (FAM)-bearing peptide is bound to the surface of the gold nanoparticle. Enzymatic cleavage of the peptide by matrix metallopeptidase-2 (MMP-2) releases FAM, which is no longer quenched. IPVSLRSG is a peptide sequence cleaved by MMP-2 at the Ser-Leu bond, with [d] representing the chelator DOTA (1,4,7,10-tetraazacyclododecane-1,4,7,10-tetraacetic acid).

b, Axial PET imaging of [^{18}F]-FDG uptake in MMP-2–overexpressing xenografts (SCC7, +) and those with xenografts expressing a low level of MMP (BT20, –) showing a non-statistically significant ($P > 0.2$) difference in uptake. ID, injected dose. **c**, CLI of the Cerenkov signal recapitulates the PET readout of [^{18}F]-FDG uptake. **d**, The activated probe can be visualized in the enzyme-expressing tumour through SCIFI using a filter for FAM, co-localizing enzyme and glycolytic activity. *$P < 0.001$. **e–g**, CL as a photon source in PDT. **e**, Cytotoxic radicals are generated in the presence of water and dissolved oxygen, from the interaction of CL with titanium dioxide nanoparticle (TiO_2) through electron–hole pair generation. **f**, CL-mediated excitation of titanocene dichloride to generate additional radicals through photofragmentation. In aerated media, the radicals transform into more-potent peroxyl radicals. **g**, Top: Schematic illustrating the development of TiO_2–PEG, TiO_2–Tf (by coating TiO_2 with transferrin, Tf) and the subsequent generation of the TiO_2–Tf–Tc construct by the simple addition of titanocene dichloride (Tc), which docks into the iron-binding site of Tf (not to scale). Bottom (left to right): transmission electron microscopy images of TiO_2–PEG, TiO_2 aggregates, TiO_2–Tf and TiO_2–Tf–Tc. Scale bars, 50 nm. Panels reproduced from ref. 27, Nature America Inc. (**a–d**) and ref. 57, Macmillan Publishers Ltd (**e–g**).

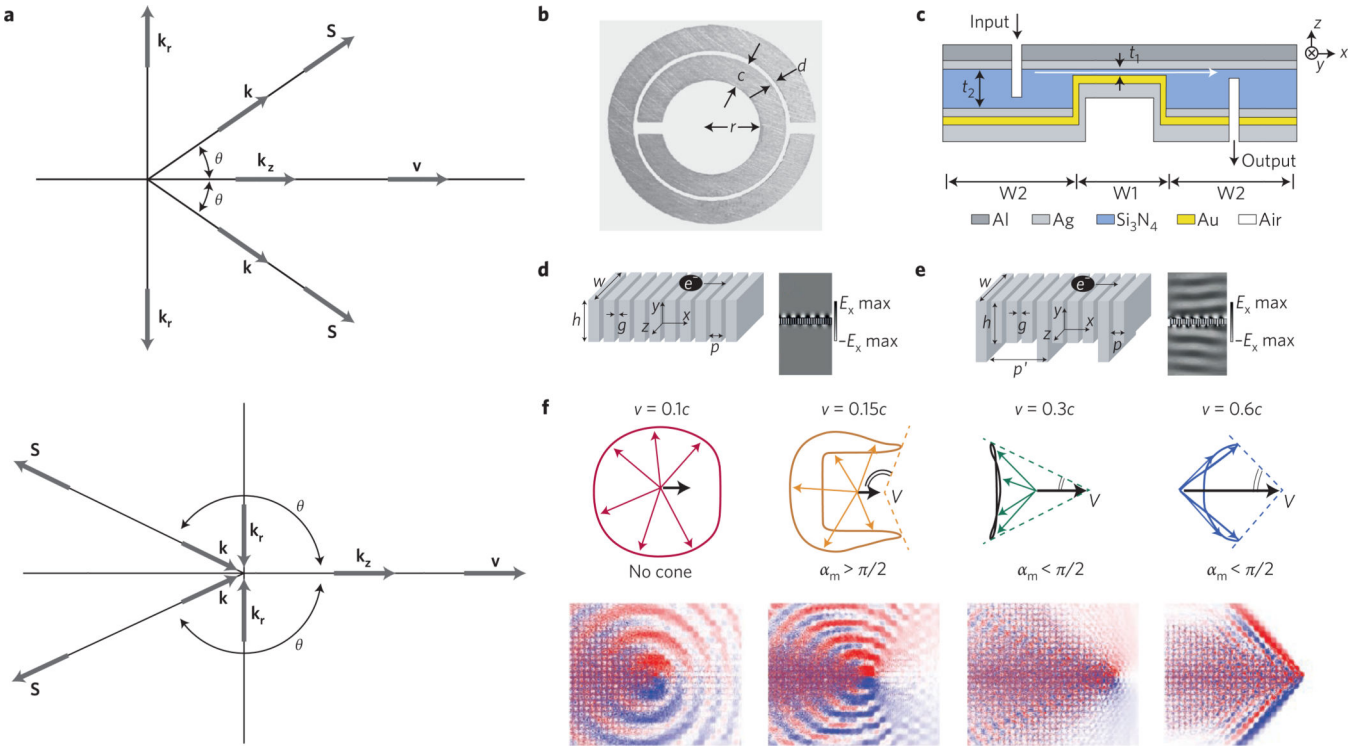

Figure 7. The Cerenkov mechanism can be modified in unique ways through interaction with metamaterials and photonic crystals

a, The Vavilov-Cherenkov effect in a positive n (top) and a left-handed n (bottom) substance, where **v** is the particle velocity, **k** is the wavevector, **S** is the Poynting vector and θ is the cone angle formed. Traditional positive n material creates a forward facing Cherenkov cone with angle θ, while negative n material produces an obtuse cone, where the cone angles in the opposite direction to the particle velocity. **b–e**, Metamaterial examples utilizing CL in practice or conceived in theory. **b**, Copper split ring resonator with dimensions: ring width c = 0.8 mm, ring spacing d = 0.2 mm and inner radius r =1.5 mm. **c**, Diagram of Au–Si_3N_4–Ag waveguide ~500 nm in height for in-plane negative refraction, where t_1, is the variable dielectric core thickness with edge angle θ, representing section W1 embedded in the waveguide of fixed core thickness t_2 = 500 nm, representing section W2. **d,e**, Metamaterial structure 1 (**d**) and structure 2 (**e**) with periodic air slits in the metal denoted, g and p, where structure 2 introduces an additional periodicity with dimensions h' and p'. Addition of periodicity amplifies the CL intensity produced in the far field (CL intensity profile right of structure design, denoted E_x) as represented by the energy density ripples at discrete angular frequencies ω. **f**, Top: finite-difference time-domain simulation results for CL in a photonic crystal. Each column represents the results for the value of velocity (v) shown on the top, where c is the speed of light in a vacuum. Overall radiation cone shapes (dashed lines) deduced from the group velocity contours where α_m is the angle of the overall radiation cone. Bottom: distribution of the radiated magnetic field. Blue, white and red represent negative, zero and positive field values, respectively. The colours have been chosen separately for best illustration in each case. Panels reproduced from ref. 63, IOP (**a**), ref. 65, APS (**b**), ref. 72, AAAS (**c**), ref. 81, OSA (**d,e**) and ref. 87, AAAS (**f**).

Table 1

Common β-emitters used in biomedical Cerenkov applications.

Radionuclide	Half-life ($t_{1/2}$)	β-decay mechanism	β_{max} (keV) [abundance %][98]	Mean photon yield per disintegration (in medium with n=1.33)[12]	Nanoparticles used *in vivo*
^{18}F	110 min	β^+	633.9 [97]	1.32	AuNP[27], QD[27,28], EO[30], $NaYF_4$[31], IONP[56], TiO_2[57]
^{64}Cu	12.7 h	β^+, β^-	653.1 [17.5], 579.4 [38.5]	0.557	QD[28,32,46,53,54], porphyrin-phospholipid NP[35], AuNP[50,52], TiO_2[57]
^{68}Ga	68 min	β^+	1,899.1 [88.9]	33.9	IONP[41]
^{89}Zr	78.4 h	β^+	902 [22.8]	2.29	QD[27], SiO_2[58]
^{90}Y	64 h	β^-	2,278.7 [100]	47.3	GdF_3:Y nanoplates[48]
^{124}I	4.18 d	β^+	1,535 [11.7], 2,138 [10.8]	8.97	AuNP[42,43], liposome[33], shell-cross-linked knedel-like NP[45]
^{177}Lu	6.71 d	β^-	0.498 [78.7], 0.112 [9.1], 0.048 [11.6]	0.141	-
^{198}Au	2.69 d	β^-	961.0 [99]	Not reported	AuNP[49]

QD, quantum dot; AuNP, gold nanoparticle; EO, europium oxide nanoparticle; $NaYF_4$, yttrium fluoride nanocrystals; IONP, iron oxide nanoparticle; TiO_2, titanium dioxide nanoparticle; SiO_2, silica nanoparticle.